

Article

Study on the Enhanced Shelf Lifetime of CYTOP-Encapsulated Organic Solar Cells

Jaehoon Kim ¹, Hyung-Jun Song ^{2,*} and Changhee Lee ^{1,*}

¹ Department of Electrical and Computer Engineering, Seoul National University, Seoul 08826, Korea; jplane@snu.ac.kr

² Department of Safety Engineering, Seoul National University of Science and Technology, Seoul 01811, Korea

* Correspondence: hj.song@seoultech.ac.kr (H.-J.S.); chlee7@snu.ac.kr (C.L.)

Abstract: Organic solar cells (OSCs) are an attractive technique for next-generation renewable energy. However, the intrinsically unstable nature of the organic compounds involved is delaying their commercialization. Therefore, it is essential to improve the lifetime of OSCs significantly. Here, we investigated the effect of the hydrophobic cyclized transparent optical polymer (CYTOP) as a solution-processable encapsulation layer based on shelf lifetime measurement, current–voltage characteristics, and impedance spectroscopy. We found that CYTOP utilization greatly enhanced OSCs' shelf lifetime, maintaining 96% of initial performance when unencapsulated devices decreased to 82%. Furthermore, based on the dark current characteristics, ideality factor (n), and Cole–Cole plots, the CYTOP encapsulation is revealed to effectively inhibit unfavorable changes of parasitic resistive components and trap-assisted recombination. These findings provide an inclusive perspective on the shelf lifetime issue and commercialization of the OSCs.

Keywords: organic solar cells; encapsulation; shelf lifetime; CYTOP



Citation: Kim, J.; Song, H.-J.; Lee, C. Study on the Enhanced Shelf Lifetime of CYTOP-Encapsulated Organic Solar Cells. *Energies* **2021**, *14*, 3993. <https://doi.org/10.3390/en14133993>

Academic Editor: Anastasia Soutati

Received: 7 June 2021

Accepted: 30 June 2021

Published: 2 July 2021

Publisher's Note: MDPI stays neutral with regard to jurisdictional claims in published maps and institutional affiliations.



Copyright: © 2021 by the authors. Licensee MDPI, Basel, Switzerland. This article is an open access article distributed under the terms and conditions of the Creative Commons Attribution (CC BY) license (<https://creativecommons.org/licenses/by/4.0/>).

1. Introduction

Since Tang, C. W. et al. first revealed an organic solar cell (OSC) with a copper phthalocyanine/perylene derivative as a light-absorbing layer [1], the OSC has been regarded as a strong candidate for next-generation renewable energy due to its unique advantages such as solution processability [2], high efficiency at low-light intensity [3], lightweight characteristics [4], and broad applicability [5]. In particular, as OSC shows excellent performance under indoor lighting [3], it would be a strong candidate for the power source of internet-of-things based sensors. Although the initial performances of OSCs were significantly lower than that of conventional Si-based solar cells [6], their chronic limitation of low efficiency is expected to be resolved shortly due to recent drastic improvements. Recently, the National Renewable Energy Laboratory (NREL)-certified solar cell efficiency of OSC has surpassed 18.2% [6]. These rapid improvements in efficiency can be attributed to several achievements, including the synthesis of state-of-the-art polymers [7], highly efficient non-fullerene acceptors [8], and advanced interfacial engineering [9–11].

Nonetheless, OSCs' commercialization has yet to be accomplished because of their premature aging caused by the intrinsically weak stability of organic materials. Normally, it is known that the π -bonds in the organic compound are vulnerable to oxidization by various external aging agents such as moisture, oxygen, heat, and light [12]. During the operation of OSCs in outdoor conditions, where intense light irradiates them and elevates their temperature, the organic materials are decomposed, and the miscibility of donor and acceptor in the bulk heterojunction layer is deformed [13]. These phenomena result in early degradation of OSCs' performance. In order to extend the operational lifetime of OSCs under high temperature and strong light irradiation, a number of studies regarding stubborn interfacial layers [14,15], stable active layer materials [16], filtering of

the ultraviolet region from the illumination [17], and improved heat dissipation [18] have been previously reported.

On the other hand, the moisture and oxygen in ambient air have a massive effect on the shelf lifetime of OSCs, which is incredibly essential, considering that the solar cells are not in a continuous working state the entire day [19–21]. Thus, encapsulation layers, to inhibit the moisture and oxygen from penetrating underneath the device structure, have been widely accepted to extend OSCs' shelf lifetime. Highly compact and protective encapsulation for the OSCs is desirable to achieve an extended shelf lifetime [22,23]. Among several techniques, using oxygen-getter-attached rigid encapsulation glass with adhesive glues is the most widely adopted method for OSCs studies because of its cost-effectiveness [24]. However, this method has some critical flaws in that it is difficult to apply to flexible devices and large panels. Therefore, various thin-film encapsulation layers through thermal evaporation and/or solution process have been developed to overcome these issues. For example, thickness-controllable and large-area-processable thin films guarantee improved stability of OSCs against moisture and oxygen via atomic layer deposition (ALD) [25,26], plasma-enhanced chemical vapor deposition (PECVD) [27], and solution processing [28,29]. In brief, a 200 nm thick Al_2O_3 layer, deposited by ALD, offered a 600-fold increase to the stability of pentacene/ C_{60} -based OSCs by effectively protecting OSCs from moisture and oxygen [26]. Poly(ethylene naphthalate) (PEN), deposited by PECVD, also offered a significant increase in OSC shelf lifetime from a few hours to over 3000 h [27]. However, these kinds of evaporative methods, including ALD or PECVD, inevitably include high-temperature and vacuum process, which causes increased manufacturing cost compared to solution processes. Hence, the development of solution-processable encapsulation layers, such as perhydropolysilazane (PHPS) [28] or cyclized transparent optical polymer (CYTOP) [29], has been motivated.

Among various solution-processable candidates, the hydrophobic polymer CYTOP has been pointed out to significantly enhance the stability of optoelectronic devices [29–31]. In brief, CYTOP is a fluoropolymer (Figure 1a) of which the hydrofluoric surface is effective for repelling moisture [29,32–34], and moisture is a representative aging factor in organic devices [12]. For example, Granstrom, J. et al. reported that a CYTOP-encapsulated organic light-emitting diode (OLED) showed minor degradation after immersion in water for 2 min, while bare devices without CYTOP layers were totally degraded [29]. Similarly, Kim, J. M. et al. revealed that CYTOP encapsulation provided strong water resistance for pentacene-based organic thin-film transistors (OTFTs), resulting in negligible change of OTFT characteristics with a drop of water placed on the channel [32]. Although a few articles have reported the encapsulation functioning of CYTOP for solar cells [30,31], a comprehensive analysis of the effect of the CYTOP encapsulation on OSCs' shelf lifetime with detailed diode characteristics and impedance spectroscopy has not been conducted. Hence, the comprehensive study of the CYTOP encapsulation layer in OSCs would provide valuable insights for designing reliable OSCs.

Herein, we provide a systematic evaluation of the effect of CYTOP encapsulation on OSCs (Figure 1). The stabilities of devices with CYTOP encapsulation were compared with those without encapsulation. The J–V characteristics of initial and shelf-stored devices revealed that CYTOP-encapsulated OSCs maintained 96% of their initial efficiency even after 35 days of shelf aging, while OSCs without encapsulation decreased to 82% of their initial efficiency (Figures 2 and 3). Further analyses concerning parasitic resistance were conducted (Figure 4 and Table 1) by characterizing the intrinsic diode curves without light illumination to calculate the serial resistive component, which reflects the degree of the aging of organic layers [35] and the effectiveness of CYTOP encapsulation. The study of ideality factor (n) extrapolated from the J–V curves [36] of devices indicates that the generation of trap-assisted recombination from oxygen and moisture was hampered by CYTOP encapsulation in the organic semiconducting layers (Figure 5). Finally, Cole–Cole plots were assessed by impedance spectroscopy in order to look at the recombination resistance component of OSCs [37,38], which is varied sensitively by the degree of aging

(Figure 6). Through the series of comprehensive electro-optical analyses, we found that CYTOP encapsulation inhibits disadvantageous degradation in OSCs, which is strongly speculated to originate from reduced moisture penetration due to the CYTOP film [29,32–34].

Table 1. Performance parameters ^{1,2} and resistive components of the CYTOP-encapsulated and bare devices before and after aging.

	CYTOP		Bare	
	Pristine	Aged	Pristine	Aged
J_{SC} (mA cm ⁻²)	12.83 ± 0.46 (13.50)	13.16 ± 0.19 (13.23)	12.67 ± 0.29 (13.08)	11.93 ± 0.29 (12.05)
V_{OC} (V)	0.75 ± 0.00 (0.75)	0.76 ± 0.00 (0.75)	0.75 ± 0.00 (0.75)	0.76 ± 0.00 (0.76)
FF	0.66 ± 0.03 (0.69)	0.62 ± 0.01 (0.61)	0.66 ± 0.01 (0.67)	0.57 ± 0.02 (0.56)
PCE (%)	6.36 ± 0.38 (6.95)	6.13 ± 0.18 (6.05)	6.32 ± 0.17 (6.60)	5.17 ± 0.18 (5.13)
R_S (Ω·cm ²)	5.5	7.3	6.7	11.3
R_{SH} (Ω·cm ²)	8.8 × 10 ²	7.3 × 10 ²	10.3 × 10 ²	5.6 × 10 ²

¹ Average and standard deviation calculated on 8 independent devices. ² The numbers in parentheses are the data of devices with the highest initial efficiency.

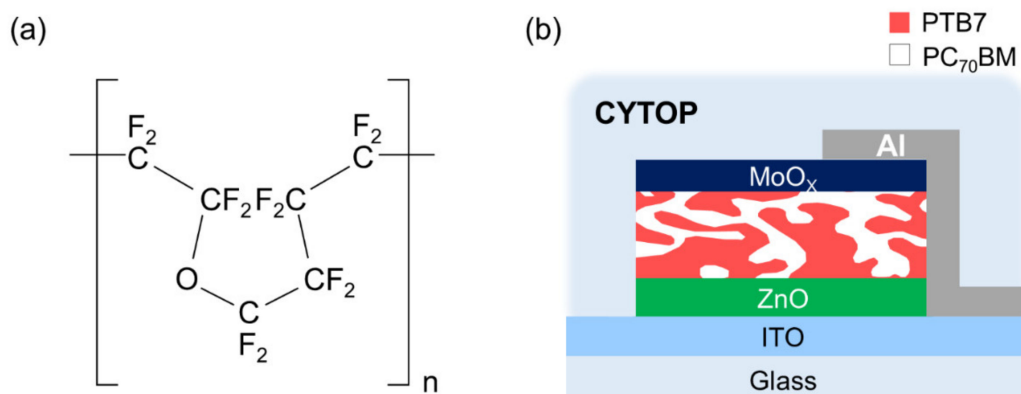


Figure 1. (a) Chemical structure of CYTOP and (b) schematic illustration of CYTOP-encapsulated organic solar cell (OSC).

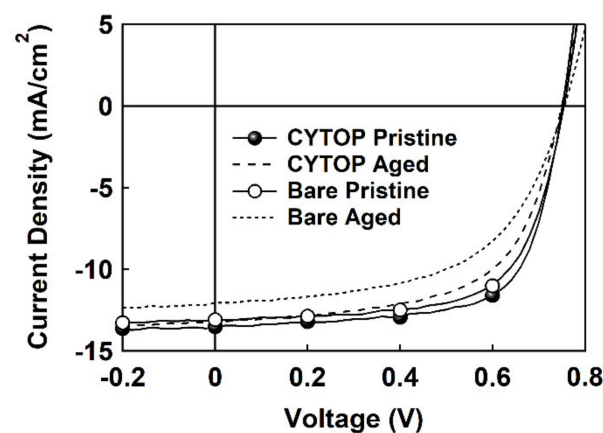


Figure 2. Current density-voltage (J-V) characteristics of CYTOP-encapsulated and bare OSCs before and after aging.

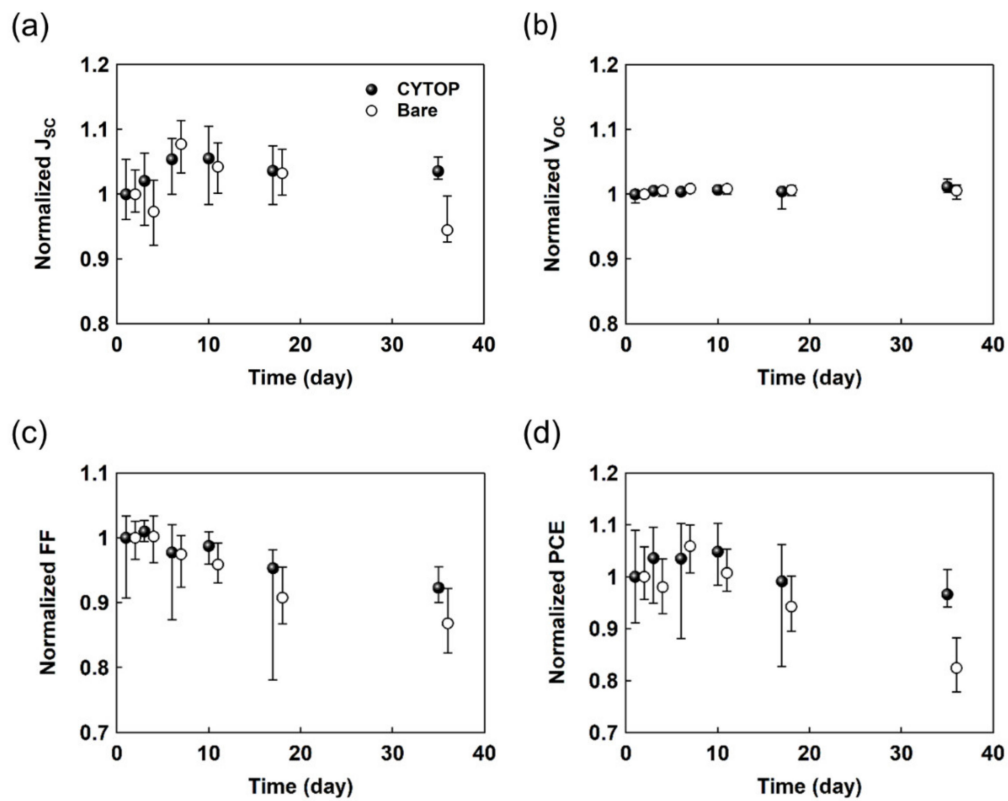


Figure 3. Normalized (a) short-circuit current (J_{SC}), (b) open-circuit voltage (V_{OC}), (c) fill factor (FF), and (d) power conversion efficiency (PCE) of CYTOP-encapsulated and bare OSCs as a function of aging time.

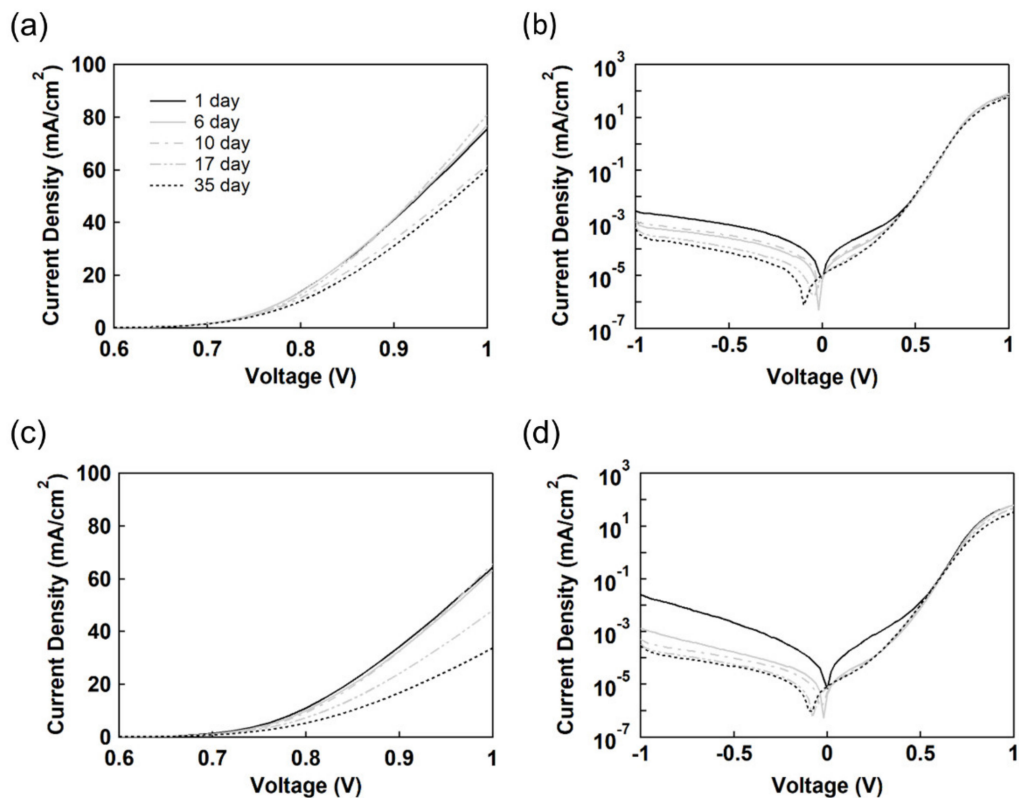


Figure 4. Linear and logarithmic current density–voltage (J - V) characteristics without the illumination of (a,b) CYTOP-encapsulated and (c,d) bare devices without illumination. Solid and dashed lines are the respective J - V characteristics of day 1 and day 35, where the grey lines are the curve of days between them.

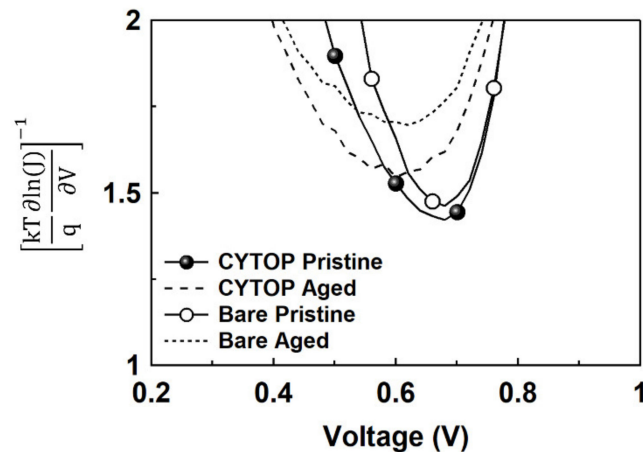


Figure 5. Ideality factor of CYTOP-encapsulated and bare OSCs extrapolated from the current density–voltage (J - V) characteristics in dark conditions.

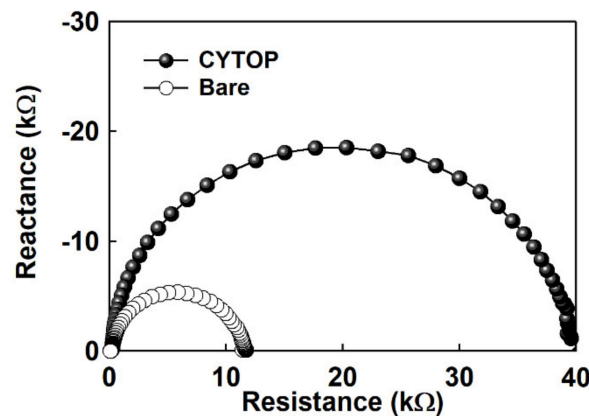


Figure 6. Cole–Cole plots of CYTOP-encapsulated and bare OSCs after 35-day shelf aging, measured by impedance spectroscopy in dark conditions.

2. Materials and Methods

The experimental details are as follows. An inverted structure was adopted for OSCs' fabrication (Figure 1b) due to its stable performance compared to the conventional structure, which generally adopts a highly acidic hole injection layer of poly(3,4-ethylenedioxythiophene) polystyrene sulfonate (PEDOT:PSS) [39] and unstable low-work electron injection layers [40,41]. The adopted OSCs' structure is as follows: indium tin oxide (ITO)/ZnO/poly[[4,8-bis[(2-ethylhexyl)oxy]benzo[1,2-b:4,5-b']dithiophene-2,6-diyl]] [3-fluoro-2-[(2-ethylhexyl)carbonyl]thieno[3,4-b]thiophenediyl]] (PTB7):[6,6]-phenyl C71 butyric acid methyl ester (PC₇₀BM)/MoO_x/Al. ITO substrates (150 nm) were rinsed with acetone, isopropyl alcohol, and deionized water, sequentially. ZnO nanoparticles were synthesized, referring to a former article [42]. In brief, the mixture of Zn(CH₃COO)₂·2H₂O (2 g) and methanol (80 mL) was annealed up to 60 °C. Then, KOH solution (1.51 g), dissolved in 65 mL of methanol, was added dropwise to the mixture, followed by stirring for 145 min. Finally, the mixture was centrifuged at 4000 rpm and redispersed in 1-butanol. After washing the ITO substrate, the prepared ZnO nanoparticle solution (20 mg·mL⁻¹) was spin-coated on the ITO substrate with 2000 rpm for 40 s, followed by annealing at 100 °C for 30 min under N₂ condition. Then, the active layer solution of PTB7:PC₇₀BM (1:2 weight ratio) (25 mg·mL⁻¹) dissolved in chlorobenzene:1,8-diiodooctane (97:3 volume ratio) was spin-coated on the ZnO film at 1000 rpm for 60 s. After active layer formation, the films were stored in a high-vacuum chamber (10⁻⁶ torr) overnight for sufficient vacuum annealing without thermal damage to the active layer. Finally, MoO_x (10 nm) and

Al (100 nm) were thermally evaporated with rates of $0.23 \text{ \AA}\cdot\text{s}^{-1}$ and $2 \text{ \AA}\cdot\text{s}^{-1}$, respectively. After fabricating the devices, CYTOP (CTL-809M, Asahi Glass Co., Ltd. Tokyo, Japan), diluted with CYTOP solvent (CTL-180, Asahi Glass Co., Ltd. Tokyo, Japan) in 83 vol%, was spin-coated on the anode at 2000 rpm for 60 sec, followed by an overnight drying in a high-vacuum chamber (10^{-6} torr). For volume concentration of 83 vol%, the CTL-809M and CTL-180 were mixed with a ratio of 5:1. According to former articles, CYTOP generally offers a thickness of 1–2 μm [43–45]. For shelf aging conditions, the devices were stored in an ambient condition without any illumination to exclude the influence of external light. During the shelf lifetime measurement, the measurement was conducted without any delay to minimize the degradation of OSCs by the light illuminated from the solar simulator. The photovoltaic parameters, including the short circuit current (J_{SC}), open-circuit voltage (V_{OC}), fill factor (FF), and power conversion efficiency (PCE), were extracted from current density–voltage (J–V) characteristics measured by a Keithley 237 (Keithley Instrument Inc. Cleveland, USA) source measurement unit equipped with an AM 1.5G solar simulator (Newport, 91160A, Irvine, USA). The Cole–Cole plots were obtained using impedance spectroscopy (6500B Series; Wayne Kerr Electronics, Bornor Regis, United Kingdom). The spectra were measured under a forward bias of 0.75 V in the frequency range of 20–50 MHz to provide an open-circuit condition. The impedance spectroscopy was measured under a dark condition to extrapolate the recombination resistance effectively [46,47].

3. Results

In Figure 2 and Table 1, the J–V characteristics of OSCs with and without CYTOP encapsulation were measured. Hereafter, we name the OSC without encapsulation as a “bare device”. Right after the fabrication, the devices showed identical performance. The CYTOP and bare devices showed average values of $J_{\text{SC}} = 12.83 \text{ mA}\cdot\text{cm}^{-2}$, $V_{\text{OC}} = 0.75 \text{ V}$, $\text{FF} = 0.66$, $\text{PCE} = 6.36\%$ and $J_{\text{SC}} = 12.67 \text{ mA}\cdot\text{cm}^{-2}$, $V_{\text{OC}} = 0.75 \text{ V}$, $\text{FF} = 0.66$, $\text{PCE} = 6.32\%$, respectively. The identical PCE of CYTOP-encapsulated and bare devices is mainly attributed to the CYTOP’s excellent chemical stability and orthogonality to general organic materials due to its fluoric nature [48–50], where the significant orthogonality prevents lower layers from damaging and reacting with it during spin-coating of the CYTOP layer. Furthermore, the absence of thermal annealing steps in the PTB7 and CYTOP layers, which owes to the low glass transition temperature of PTB7 [51], is also speculated to be one reason for the similar values. To verify the encapsulating effect of the CYTOP on OSCs, the devices were exposed to an ambient air condition for 35 days without any light illumination. After the 35 days of shelf lifetime testing, they differed significantly in terms of photovoltaic parameters. While average parameters of bare devices dropped to $J_{\text{SC}} = 11.93 \text{ mA}\cdot\text{cm}^{-2}$, $V_{\text{OC}} = 0.76 \text{ V}$, $\text{FF} = 0.57$, $\text{PCE} = 5.17\%$, those of CYTOP-encapsulated devices only decreased to $J_{\text{SC}} = 13.16 \text{ mA}\cdot\text{cm}^{-2}$, $V_{\text{OC}} = 0.76 \text{ V}$, $\text{FF} = 0.62$, $\text{PCE} = 6.13\%$, of which the average PCE retained 96% of its initial value. Particularly, while V_{OC} showed no degradation regardless of encapsulation, J_{SC} and FF showed severely different stability in relation to the encapsulation condition. As reported previously, exposure to air significantly degrades OSCs’ performance, as the moisture and oxygen in the ambient air oxidizes and deteriorates the π -bond of organic compounds [52,53]. For the increased shelf lifetime of CYTOP-encapsulated devices (Figure 2 and Table 1), we speculate that it is mainly attributed to the reduced moisture penetration [29,32–34] since former articles have suggested that CYTOP relatively lacks oxygen-repelling ability compared to moisture-repelling ability [54–56].

For further insight, eight identical devices were fabricated, and their shelf lifetimes were evaluated as a function of aging time (Figure 3). V_{OC} showed no difference, with negligible deviation regardless of device conditions, whereas J_{SC} and FF differed mainly depending on the existence of CYTOP encapsulation. The CYTOP-encapsulated device sustained its initial J_{SC} and FF during the test. On the other hand, J_{SC} and FF of bare devices decreased during the test. Specifically, the J_{SC} and FF of CYTOP-encapsulated devices maintained 103% and 94% of their initial values, leading to 96% of their initial PCE. In other words, the CYTOP-encapsulated devices showed almost negligible premature aging,

which indicates that the CYTOP encapsulation layer protected the device from moisture and oxygen. In contrast, bare devices offered 94% and 86% of their J_{SC} and FF; their total PCE dropped to 82% of its initial value. Since the FF is highly affected by the series resistance (R_S) and shunt resistance (R_{SH}) [57], the significant difference in FF between the two devices is related to the different R_S and R_{SH} variations upon aging. Through calculating the reverse slope at the voltage of V_{OC} (x-intercept) [57], the R_S of CYTOP and bare devices changed from $5.5 \Omega \cdot \text{cm}^2$ and $6.7 \Omega \cdot \text{cm}^2$ to $7.3 \Omega \cdot \text{cm}^2$ and $11.3 \Omega \cdot \text{cm}^2$, respectively. While the CYTOP-encapsulated device's R_S increased by 33% after aging, the bare device's R_S increased by 70%. Similarly, calculating the reverse slope at the voltage of J_{SC} (y-intercept) [57], the R_{SH} of CYTOP and bare devices changed from $8.8 \times 10^2 \Omega \cdot \text{cm}^2$ and $10.3 \times 10^2 \Omega \cdot \text{cm}^2$ to $7.3 \times 10^2 \Omega \cdot \text{cm}^2$ and $5.6 \times 10^2 \Omega \cdot \text{cm}^2$, respectively. Compared to the initial R_{SH} of each device, a 17% decrease of R_{SH} was observed in the CYTOP-encapsulated device after the aging test, while the bare device suffered from a 46% reduction of R_{SH} . Considering that the variation of R_S and R_{SH} of the OSCs during the aging test is attributed to the degradation of organic layers due to moisture in ambient air, the different J–V characteristics indicate the superior encapsulating effect of CYTOP (please see Figure 2). For an in-depth analysis of the impact of the CYTOP thickness on the shelf lifetime, the degradation of OSCs encapsulated with CYTOP with different concentrations was analyzed, as marked in Figure S1. Compared to the bare devices, the CYTOP-encapsulated devices showed significantly improved stability regardless of CYTOP concentration, maintaining their normalized PCE over 0.9 after 35 days of the aging test. Further study about the thin CYTOP layer will allow us to find the optimized thickness of CYTOP for reliable OSCs. Therefore, we can conclude that the adopted concentration of the CYTOP was sufficient to encapsulate the devices effectively.

To further study the effect of the CYTOP encapsulation on the OSC's electrical characteristics, diode curves in dark conditions were analyzed. In Figure 4, the J–V curves of CYTOP-encapsulated and bare devices were evaluated under dark conditions. Hereafter, we name J–V characteristics in dark conditions as “dark current”. The dark current of OSC is defined as the following equation:

$$I = I_0 \cdot \left[\exp\left(\frac{V - IR_S}{V_{th}}\right) - 1 \right] + \frac{V - IR_S}{R_{SH}} \quad (1)$$

where I is the diode current, I_0 is the saturation current, V_{th} is the threshold voltage, V is the applied voltage, R_S is the series resistance, and R_{SH} is the shunt resistance. As shown in the equation, the J–V curves of OSC are affected by parasitic resistance elements. Therefore, a more considerable drop in the dark current curve is ascribed to an enormous parasitic series resistance rise, which agrees with the results discussed in the previous paragraphs (Table 1). The CYTOP-encapsulated device's dark current showed a variation of current density, measured at 1 V, from $75.51 \text{ mA} \cdot \text{cm}^{-2}$ to $60.20 \text{ mA} \cdot \text{cm}^{-2}$, whereas the bare device's curve changed from $64.29 \text{ mA} \cdot \text{cm}^{-2}$ to $33.83 \text{ mA} \cdot \text{cm}^{-2}$, which is in good agreement with the devices' calculated R_S in the previous paragraph (Table 1). To verify the different R_{SH} upon CYTOP encapsulation, further analyses of ideality factor (n) and impedance spectroscopy were conducted.

The ideality factor (n) was extrapolated based on the J–V characteristics, which provides helpful clues regarding trap-assisted recombination. According to a former article, the ideality factor (n) reflects the degree of trap-assisted recombination within the OSCs [58]. In brief, the ideality factor (n) shows a close value of unity in an ideal case, where no trap-assisted recombination but only bimolecular recombination occurs. However, when trap-assisted recombination becomes involved, the ideality factor (n) increases from 1 to 2 at the maximum. The ideality factor (n) is calculated based on the following equation:

$$n = \left(\frac{kT}{q} \frac{\partial \ln(J)}{\partial V} \right)^{-1} \quad (2)$$

where k is the Boltzmann constant, T is the absolute temperature in Kelvin, J is the current density, and V is the voltage. In Figure 5, the pristine ideality factor (n) of bare and CYTOP-encapsulated devices showed almost similar values of 1.46 and 1.42, respectively. After degradation, the ideality factor (n) of the bare device increased from 1.46 to 1.70, while the ideality factor (n) of CYTOP-encapsulated devices slightly changed (from 1.42 to 1.55). The changed ideality factor (n) after the aging test indicates that trap-assisted recombination loss becomes more dominant in the bare device compared to its initial state. As a result, more photo-generated carriers might be annihilated at the trap sites during their transport to the electrode in the bare devices after the aging test. On the other hand, the recombination process of charges is relatively maintained in the CYTOP-encapsulated OSCs, leading to slightly changed diode characteristics after the aging test. Therefore, it can be interpreted that the stable performance (Figure 3) and J–V characteristics (Figure 4) of CYTOP-encapsulated OSCs are highly related to the different degrees of change in the ideality factor (n) upon degradation, implying the excellent moisture barrier impact of CYTOP.

Compared to R_S , which sensitively affects the diode behavior at the forward bias region (Figure 4), R_{SH} generally rules the curve at lower bias voltage around near zero voltage. Among several measurements, Cole–Cole plots have been frequently used in the study of OSCs because of their clear correlation between parasitic resistance and device characteristics [38]. Exceptionally, assuming that OSCs' equivalent circuit equals serial components consisting of series resistance and several parallel $R \parallel C$ (Resistance \parallel Capacitance) components, the plot can provide a comprehensive insight into the phenomena inside the device. In Figure 6, the Cole–Cole plots of 35-day aged bare and CYTOP-encapsulated devices were measured by impedance spectroscopy with a frequency range from 20 Hz to 50 MHz. Considering that resistance at the low-frequency end of this range has a positive correlation with recombination resistance [46,59,60], the CYTOP-encapsulated device showed a larger recombination resistance (40 k Ω) than the bare device (11 k Ω), which is in line with the trends of the R_{SH} calculated from the slope of the J–V curves (Figure 2 and Table 1). In contrast to studies relating the decrease in recombination resistance under light illumination to improved charge transport [61], some articles correlated the increase in recombination resistance under a dark condition with reduced charge recombination within the device's bulk and interface [62], which is interpreted to be the case in Figure 6. As discussed in the previous paragraphs, the difference is speculated to originate from the degradation of organic compounds in the bare device, where the oxidation and aging of π -bonds results in severe parasitic shunt formation. On the contrary, the CYTOP-encapsulated device showed almost no aging in device characteristics due to the superior encapsulation of CYTOP (Figure 3).

4. Conclusions

Throughout the study, we systematically studied the effect of CYTOP encapsulation on OSCs' performance by analyzing J–V characteristics, shelf lifetime, dark current, ideality factor (n), and Cole–Cole plots. While CYTOP-encapsulated and bare devices showed identical performance at the initial state due to the significant orthogonality of CYTOP, they showed significant differences after 35-day shelf storage. CYTOP-encapsulated devices maintained their performance (96% of initial efficiency), whereas the efficiency of bare devices without encapsulation layers dropped to 82% (Figures 2 and 3). Electro-optical characteristic analysis of OSCs with and without encapsulation layers indicates that moisture penetrating the organic semiconducting layer of OSCs acts as recombination center and deteriorates diode characteristics of OSCs. However, the suggested CYTOP encapsulation layer effectively provides moisture and humidity barriers to OSCs during the shelf aging test, thereby preserving OSCs' performance. Additional analyses of the R_S/R_{SH} (Figures 2 and 4, and Table 1), ideality factor (n) (Figure 5), and recombination resistance of OSCs (Figure 6) depending on encapsulation conditions confirm that the introduction of CYTOP encapsulation layers to OSCs enables them to withstand moisture and oxygen

and maintain their diode characteristics. We believe that this study gives a comprehensive view on resolving the intrinsically weak stability of OSCs.

Supplementary Materials: The following are available online at <https://www.mdpi.com/article/10.3390/en14133993/s1>, Figure S1: Normalized power conversion efficiency of OSC with different volume concentration CYTOP layer.

Author Contributions: Conceptualization, writing—review and editing, supervision, H.-J.S. and C.L.; validation, investigation, writing, visualization, J.K. All authors have read and agreed to the published version of the manuscript.

Funding: This research was funded by the Mid-career Researcher Program (2016R1A2B3009301), the Basic Science Research Program (2019R1F1A1057693) through the National Research Foundation of Korea (NRF) and the Ministry of Trade, Industry, and Energy of Korea (MOTIE,10077471, 20015773).

Data Availability Statement: Data is contained within the article.

Conflicts of Interest: The authors declare no conflict of interest. The funders had no role in the design of the study; in the collection, analyses, or interpretation of data; in the writing of the manuscript, or in the decision to publish the results.

References

1. Tang, C.W. Two-layer organic photovoltaic cell. *Appl. Phys. Lett.* **1986**, *48*, 183–185. [[CrossRef](#)]
2. Hori, T.; Miyake, Y.; Yamasaki, N.; Yoshida, H.; Fujii, A.; Shimizu, Y.; Ozaki, M. Solution processable organic solar cell based on bulk heterojunction utilizing phthalocyanine derivative. *Appl. Phys. Express* **2010**, *3*, 101602. [[CrossRef](#)]
3. Steim, R.; Ameri, T.; Schilinsky, P.; Waldauf, C.; Dennler, G.; Scharber, M.; Brabec, C.J. Organic photovoltaics for low light applications. *Sol. Energy Mater. Sol. Cells* **2011**, *95*, 3256–3261. [[CrossRef](#)]
4. Kaltenbrunner, M.; White, M.S.; Glowacki, E.D.; Sekitani, T.; Someya, T.; Sariciftci, N.S.; Bauer, S. Ultrathin and lightweight organic solar cells with high flexibility. *Nat. Commun.* **2012**, *3*, 770. [[CrossRef](#)] [[PubMed](#)]
5. Peng, Y.; Zhang, L.; Cheng, N.; Andrew, T.L. ITO-Free transparent organic solar cell with distributed bragg reflector for solar harvesting windows. *Energies* **2017**, *10*, 707. [[CrossRef](#)]
6. National Renewable Energy Laboratory. Available online: <https://www.nrel.gov/pv/cell-efficiency.html> (accessed on 22 June 2021).
7. Liu, X.; Liang, Z.; Du, S.; Tong, J.; Li, J.; Zhang, R.; Shi, X.; Yan, L.; Bao, X.; Xia, Y. Non-halogenated polymer donor-based organic solar cells with a nearly 15% efficiency enabled by a classic ternary strategy. *ACS Appl. Energy Mater.* **2021**, *4*, 1774–1783. [[CrossRef](#)]
8. Chai, G.; Chang, Y.; Zhang, J.; Xu, X.; Yu, L.; Zou, X.; Li, X.; Chen, Y.; Luo, S.; Liu, B.; et al. Fine-tuning of side-chain orientations on nonfullerene acceptors enables organic solar cells with 17.7% efficiency. *Energy Environ. Sci.* **2021**, *14*, 3469–3479. [[CrossRef](#)]
9. Wang, Y.; Liang, Z.; Li, X.; Qin, J.; Ren, M.; Yang, C.; Bao, X.; Xia, Y.; Li, J. Self-doping n-type polymer as a cathode interface layer enables efficient organic solar cells by increasing built-in electric field and boosting interface contact. *J. Mater. Chem. C* **2019**, *7*, 11152–11159. [[CrossRef](#)]
10. Park, S.; Kang, R.; Cho, S. Effect of an Al-doped ZnO electron transport layer on the efficiency of inverted bulk heterojunction solar cells. *Curr. Appl. Phys.* **2020**, *20*, 172–177. [[CrossRef](#)]
11. Walker, B.; Choi, H.; Kim, J.Y. Interfacial engineering for highly efficient organic solar cells. *Curr. Appl. Phys.* **2017**, *17*, 370–391. [[CrossRef](#)]
12. Cheng, P.; Zhan, X. Stability of organic solar cells: Challenges and strategies. *Chem. Soc. Rev.* **2016**, *45*, 2544–2582. [[CrossRef](#)] [[PubMed](#)]
13. Levitsky, A.; Schneider, S.A.; Rabkin, E.; Toney, M.F.; Frey, G.L. Bridging the thermodynamics and kinetics of temperature-induced morphology evolution in polymer/fullerene organic solar cell bulk heterojunction. *Mater. Horiz.* **2021**, *8*, 1272–1285. [[CrossRef](#)]
14. Kim, J.; Lee, Y.; Kim, J.Y.; Song, H.-J.; Song, J.; Lee, H.; Lee, C. Analysis of the improved thermal stability of Al-doped ZnO-adopted organic solar cells. *Appl. Phys. Lett.* **2021**, *118*, 023302. [[CrossRef](#)]
15. Prosa, M.; Tessarolo, M.; Bolognesi, M.; Margeat, O.; Gedefaw, D.; Gaceur, M.; Videlot-Ackermann, C.; Andersson, M.R.; Muccini, M.; Seri, M.; et al. Enhanced Ultraviolet Stability of Air-Processed Polymer Solar Cells by Al Doping of the ZnO Interlayer. *ACS Appl. Mater. Interfaces* **2016**, *8*, 1635–1643. [[CrossRef](#)]
16. Nam, C.-Y.; Qin, Y.; Park, Y.S.; Hlaing, H.; Lu, X.; Ocko, B.M.; Black, C.T.; Grubbs, R.B. Photo-Cross-Linkable Azide-Functionalized Polythiophene for Thermally Stable Bulk Heterojunction Solar Cells. *Macromolecules* **2012**, *45*, 2338–2347. [[CrossRef](#)]
17. Sun, H.; Weickert, J.; Hesse, H.C.; Schmidt-Mende, L. UV light protection through TiO₂ blocking layers for inverted organic solar cells. *Sol. Energy Mater. Sol. Cells* **2011**, *95*, 3450–3454. [[CrossRef](#)]
18. Yin, H.; Chiu, K.L.; Bi, P.; Li, G.; Yan, C.; Tang, H.; Zhang, C.; Xiao, Y.; Zhang, H.; Yu, W.; et al. Enhanced electron transport and heat transfer boost light stability of ternary organic photovoltaic cells incorporating non-fullerene small molecule and polymer acceptors. *Adv. Electron. Mater.* **2019**, *5*, 1900497. [[CrossRef](#)]

19. Wang, X.; Xinxin Zhao, C.; Xu, G.; Chen, Z.-K.; Zhu, F. Degradation mechanisms in organic solar cells: Localized moisture encroachment and cathode reaction. *Sol. Energy Mater. Sol. Cells* **2012**, *104*, 1–6. [[CrossRef](#)]
20. Arredondo, B.; Romero, B.; Beliatas, M.J.; del Pozo, G.; Martín-Martín, D.; Blakesley, J.C.; Dibb, G.; Krebs, F.C.; Gevorgyan, S.A.; Castro, F.A. Analysing impact of oxygen and water exposure on roll-coated organic solar cell performance using impedance spectroscopy. *Sol. Energy Mater. Sol. Cells* **2018**, *176*, 397–404. [[CrossRef](#)]
21. Weiss, A.; Hays, C.J. Simulation of daily solar irradiance. *Agric. For. Meteorol.* **2004**, *123*, 187–199. [[CrossRef](#)]
22. Kim, N.; Potscavage, W.J.; Sundaramoorthi, A.; Henderson, C.; Kippelen, B.; Graham, S. A correlation study between barrier film performance and shelf lifetime of encapsulated organic solar cells. *Sol. Energy Mater. Sol. Cells* **2012**, *101*, 140–146. [[CrossRef](#)]
23. Gevorgyan, S.A.; Madsen, M.V.; Roth, B.; Corazza, M.; Hösel, M.; Søndergaard, R.R.; Jørgensen, M.; Krebs, F.C. Lifetime of Organic Photovoltaics: Status and Predictions. *Adv. Energy Mater.* **2016**, *6*, 1501208. [[CrossRef](#)]
24. Giannouli, M.; Drakonakis, V.M.; Savva, A.; Eleftheriou, P.; Florides, G.; Choulis, S.A. Methods for improving the lifetime performance of organic photovoltaics with low-costing encapsulation. *ChemPhysChem* **2015**, *16*, 1134–1154. [[CrossRef](#)] [[PubMed](#)]
25. Sarkar, S.; Culp, J.H.; Whyland, J.T.; Garvan, M.; Misra, V. Encapsulation of organic solar cells with ultrathin barrier layers deposited by ozone-based atomic layer deposition. *Org. Electron.* **2010**, *11*, 1896–1900. [[CrossRef](#)]
26. Potscavage, W.J.; Yoo, S.; Domercq, B.; Kippelen, B. Encapsulation of pentacene/C60 organic solar cells with Al₂O₃ deposited by atomic layer deposition. *Appl. Phys. Lett.* **2007**, *90*, 253511. [[CrossRef](#)]
27. Dennler, G.; Lungenschmied, C.; Neugebauer, H.; Sariciftci, N.S.; Latrèche, M.; Czeremuszkin, G.; Wertheimer, M.R. A new encapsulation solution for flexible organic solar cells. *Thin Solid Films* **2006**, *511*, 349–353. [[CrossRef](#)]
28. Channa, I.A.; Distler, A.; Zaiser, M.; Brabec, C.J.; Egelhaaf, H.-J. Thin film encapsulation of organic solar cells by direct deposition of polysilazanes from solution. *Adv. Energy Mater.* **2019**, *9*, 1900598. [[CrossRef](#)]
29. Granstrom, J.; Swensen, J.S.; Moon, J.S.; Rowell, G.; Yuen, J.; Heeger, A.J. Encapsulation of organic light-emitting devices using a perfluorinated polymer. *Appl. Phys. Lett.* **2008**, *93*, 193304. [[CrossRef](#)]
30. Zheng, Y.; Shi, W.; Kong, J.; Huang, D.; Katz, H.E.; Yu, J.; Taylor, A.D. A cytop insulating tunneling layer for efficient perovskite solar cells. *Small Methods* **2017**, *1*, 1700244. [[CrossRef](#)]
31. Chang, C.-Y.; Wang, C.-C. Enhanced stability and performance of air-processed perovskite solar cells via defect passivation with a thiazole-bridged diketopyrrolopyrrole-based π -conjugated polymer. *J. Mater. Chem. A* **2020**, *8*, 8593–8604. [[CrossRef](#)]
32. Kim, J.M.; Oh, J.; Jung, K.-M.; Park, K.; Jeon, J.-H.; Kim, Y.-S. Ultrathin flexible thin film transistors with CYTOP encapsulation by debonding process. *Semicond. Sci. Technol.* **2019**, *34*, 075015. [[CrossRef](#)]
33. Jeon, P.J.; Min, S.-W.; Kim, J.S.; Raza, S.R.A.; Choi, K.; Lee, H.S.; Lee, Y.T.; Hwang, D.K.; Choi, H.J.; Im, S. Enhanced device performances of WSe₂–MoS₂ van der Waals junction p–n diode by fluoropolymer encapsulation. *J. Mater. Chem. C* **2015**, *3*, 2751–2758. [[CrossRef](#)]
34. Seo, S.G.; Jin, S.H. Bias Temperature Stress Instability of Multilayered MoS₂ Field-Effect Transistors with CYTOP Passivation. *IEEE Trans. Electron Devices* **2019**, *66*, 2208–2213. [[CrossRef](#)]
35. Lare, Y.; Kouskoussa, B.; Benchouk, K.; Ouro Djobo, S.; Cattin, L.; Morsli, M.; Diaz, F.R.; Gacitua, M.; Abachi, T.; del Valle, M.A.; et al. Influence of the exciton blocking layer on the stability of layered organic solar cells. *J. Phys. Chem. Solids* **2011**, *72*, 97–103. [[CrossRef](#)]
36. Na, I.; Lee, S.E.; Joo, M.-K.; Park, I.-H.; Song, J.-I.; Joo, H.; Kim, Y.K.; Kim, G.-T. Effect of Ir(pq)₂acac doping on CBP in phosphorescence organic light-emitting diodes. *Curr. Appl. Phys.* **2020**, *20*, 78–81. [[CrossRef](#)]
37. Qi, B.; Zhang, Z.-G.; Wang, J. Uncovering the role of cathode buffer layer in organic solar cells. *Sci. Rep.* **2015**, *5*, 7803. [[CrossRef](#)]
38. Li, Z.; Guo, W.; Liu, C.; Zhang, X.; Li, S.; Guo, J.; Zhang, L. Impedance investigation of the highly efficient polymer solar cells with composite CuBr₂/MoO₃ hole transport layer. *Phys. Chem. Chem. Phys.* **2017**, *19*, 20839–20846. [[CrossRef](#)]
39. Zhang, Y.; Chen, L.; Hu, X.; Zhang, L.; Chen, Y. Low Work-function Poly(3,4-ethylenedioxythiophene): Poly(styrene sulfonate) as Electron-transport Layer for High-efficient and Stable Polymer Solar Cells. *Sci. Rep.* **2015**, *5*, 12839. [[CrossRef](#)]
40. De Jong, M.P.; Van Ijzendoorn, L.J.; De Voigt, M.J.A. Stability of the interface between indium-tin-oxide and poly(3,4-ethylenedioxythiophene)/poly(styrenesulfonate) in polymer light-emitting diodes. *Appl. Phys. Lett.* **2000**, *77*, 2255–2257. [[CrossRef](#)]
41. Greczynski, G.; Kugler, T.; Keil, M.; Osikowicz, W.; Fahlman, M.; Salaneck, W.R. Photoelectron spectroscopy of thin films of PEDOT–PSS conjugated polymer blend: A mini-review and some new results. *J. Electron Spectrosc. Relat. Phenom.* **2001**, *121*, 1–17. [[CrossRef](#)]
42. Lim, J.; Park, M.; Bae, W.K.; Lee, D.; Lee, S.; Lee, C.; Char, K. Highly Efficient cadmium-free quantum dot light-emitting diodes enabled by the direct formation of excitons within InP@ZnSeS quantum dots. *ACS Nano* **2013**, *7*, 9019–9026. [[CrossRef](#)] [[PubMed](#)]
43. Lu, J.; Zhang, L.; Takagi, H.; Maeda, R. Cavity-first approach for microelectromechanical system–CMOS monolithic integration. *Micro Nano Lett.* **2013**, *8*, 700–703. [[CrossRef](#)]
44. Schmidt, G.C.; Höft, D.; Haase, K.; Hübler, A.C.; Karpov, E.; Tkachov, R.; Stamm, M.; Kiriy, A.; Haidu, F.; Zahn, D.R.T.; et al. Naphtalenediimide-based donor–acceptor copolymer prepared by chain-growth catalyst-transfer polycondensation: Evaluation of electron-transporting properties and application in printed polymer transistors. *J. Mater. Chem. C* **2014**, *2*, 5149–5154. [[CrossRef](#)]
45. Han, A.; Oh, K.W.; Bhansali, S.; Henderson, H.T.; Ahn, C.H. A low temperature biochemically compatible bonding technique using fluoropolymers for biochemical microfluidic systems. In Proceedings of the IEEE Thirteenth Annual International Conference on Micro Electro Mechanical Systems, Miyazaki, Japan, 23–27 January 2000; pp. 414–418.

46. Arredondo, B.; Romero, B.; Del Pozo, G.; Sessler, M.; Veit, C.; Würfel, U. Impedance spectroscopy analysis of small molecule solution processed organic solar cell. *Sol. Energy Mater. Sol. Cells* **2014**, *128*, 351–356. [[CrossRef](#)]
47. Kobori, T.; Kamata, N.; Fukuda, T. Impedance spectroscopy for annealing-induced change of molybdenum oxide in organic photovoltaic cell. *Adv. Mater. Phys. Chem.* **2017**, *7*, 323–333. [[CrossRef](#)]
48. Bulgarevich, K.; Sakamoto, K.; Yasuda, T.; Minari, T.; Takeuchi, M. Operational stability enhancement of polymeric organic field-effect transistors by amorphous perfluoropolymers chemically anchored to gate dielectric surfaces. *Adv. Electron. Mater.* **2020**, *6*, 2000161. [[CrossRef](#)]
49. Hamilton, R.; Smith, J.; Ogier, S.; Heeney, M.; Anthony, J.E.; McCulloch, I.; Veres, J.; Bradley, D.D.C.; Anthopoulos, T.D. High-performance polymer-small molecule blend organic transistors. *Adv. Mater.* **2009**, *21*, 1166–1171. [[CrossRef](#)]
50. Hwang, D.K.; Fuentes-Hernandez, C.; Kim, J.; Potscavage, W.J., Jr.; Kim, S.-J.; Kippelen, B. Top-gate organic field-effect transistors with high environmental and operational stability. *Adv. Mater.* **2011**, *23*, 1293–1298. [[CrossRef](#)]
51. Root, S.E.; Jackson, N.E.; Savagatrup, S.; Arya, G.; Lipomi, D.J. Modelling the morphology and thermomechanical behaviour of low-bandgap conjugated polymers and bulk heterojunction films. *Energy Environ. Sci.* **2017**, *10*, 558–569. [[CrossRef](#)]
52. Seemann, A.; Sauermann, T.; Lungenschmied, C.; Armbruster, O.; Bauer, S.; Egelhaaf, H.J.; Hauch, J. Reversible and irreversible degradation of organic solar cell performance by oxygen. *Sol. Energy* **2011**, *85*, 1238–1249. [[CrossRef](#)]
53. Yamilova, O.R.; Martynov, I.V.; Brandvold, A.S.; Klimovich, I.V.; Balzer, A.H.; Akkuratov, A.V.; Kusnetsov, I.E.; Stingelin, N.; Troshin, P.A. What is Killing Organic Photovoltaics: Light-Induced Crosslinking as a General Degradation Pathway of Organic Conjugated Molecules. *Adv. Energy Mater.* **2020**, *10*, 1903163. [[CrossRef](#)]
54. Harwell, J.R.; Whitworth, G.L.; Turnbull, G.A.; Samuel, I.D.W. Green Perovskite Distributed Feedback Lasers. *Sci. Rep.* **2017**, *7*, 11727. [[CrossRef](#)]
55. Sun, Q.; Liu, X.; Cao, J.; Stantchev, R.I.; Zhou, Y.; Chen, X.; Parrott, E.P.J.; Lloyd-Hughes, J.; Zhao, N.; Pickwell-MacPherson, E. Highly Sensitive Terahertz Thin-Film Total Internal Reflection Spectroscopy Reveals in Situ Photoinduced Structural Changes in Methylammonium Lead Halide Perovskites. *J. Phys. Chem. C* **2018**, *122*, 17552–17558. [[CrossRef](#)]
56. Hwang, D.K.; Fuentes-Hernandez, C.; Fenoll, M.; Yun, M.; Park, J.; Shim, J.W.; Knauer, K.A.; Dindar, A.; Kim, H.; Kim, Y.; et al. Systematic reliability study of top-gate p- and n-channel organic field-effect transistors. *ACS Appl. Mater. Interfaces* **2014**, *6*, 3378–3386. [[CrossRef](#)] [[PubMed](#)]
57. Qi, B.; Wang, J. Fill factor in organic solar cells. *Phys. Chem. Chem. Phys.* **2013**, *15*, 8972–8982. [[CrossRef](#)] [[PubMed](#)]
58. Kyaw, A.K.K.; Wang, D.H.; Gupta, V.; Leong, W.L.; Ke, L.; Bazan, G.C.; Heeger, A.J. Intensity dependence of current–voltage characteristics and recombination in high-efficiency solution-processed small-molecule solar cells. *ACS Nano* **2013**, *7*, 4569–4577. [[CrossRef](#)] [[PubMed](#)]
59. Guerrero, A.; Montcada, N.F.; Ajuria, J.; Etxebarria, I.; Pacios, R.; Garcia-Belmonte, G.; Palomares, E. Charge carrier transport and contact selectivity limit the operation of PTB7-based organic solar cells of varying active layer thickness. *J. Mater. Chem. A* **2013**, *1*, 12345–12354. [[CrossRef](#)]
60. Yao, E.-P.; Chen, C.-C.; Gao, J.; Liu, Y.; Chen, Q.; Cai, M.; Hsu, W.-C.; Hong, Z.; Li, G.; Yang, Y. The study of solvent additive effects in efficient polymer photovoltaics via impedance spectroscopy. *Sol. Energy Mater. Sol. Cells* **2014**, *130*, 20–26. [[CrossRef](#)]
61. Kim, J.Y.; Vincent, P.; Jang, J.; Jang, M.S.; Choi, M.; Bae, J.-H.; Lee, C.; Kim, H. Versatile use of ZnO interlayer in hybrid solar cells for self-powered near infra-red photo-detecting application. *J. Alloys Compd.* **2020**, *813*, 152202. [[CrossRef](#)]
62. Jin, M.-J.; Jo, J.; Yoo, J.-W. Impedance spectroscopy analysis on the effects of TiO₂ interfacial atomic layers in ZnO nanorod polymer solar cells: Effects of interfacial charge extraction on diffusion and recombination. *Org. Electron.* **2015**, *19*, 83–91. [[CrossRef](#)]